Collective properties of neutron-deficient Nd isotopes: Lifetime measurements of the yrast states in ^{136}Nd

A. Turturică,[1,2] C. Costache,[1,2] P. Petkov,[1] J.-P. Delaroche,[3] M. Girod,[3] J. Libert,[3] G. Cată-Danil,[2] S. Pascu,[1] C. Mihai,[1] M. Boromiza,[1] D. Bucurescu,[1] C. Clisu,[1] D. Filipescu,[1] N. M. Florea,[1] I. Gheorghe,[1] A. Ionescu,[1,4] R. Lică,[1] N. M. Mărginean,[1] R. Mărginean,[1] R. E. Mihai,[1] A. Mitu,[1] A. Negret,[1] C. R. Niţă,[1] A. Olăcel,[1] A. Oprea,[1] T. Sava,[1] C. Sotty,[1] L. Stan,[1,2] I. Ştiru,[1,2] R. Şuvăilă,[1] S. Toma,[1,2] G. V. Turturică,[2,5] and S. Ujeniuc[1,2]

[1]*Horia Hulubei National Institute of Physics and Nuclear Engineering, RO-077125 Bucharest, Romania*
[2]*Physics Department, University "Politehnica" of Bucharest, Bucharest, Romania*
[3]*CEA, DAM, DIF, F-91297 Arpajon, France*
[4]*University of Bucharest, Faculty of Physics, Magurele, Romania*
[5]*ELI-NP – Horia Hulubei National Institute for R&D in Physics and Nuclear Engineering, Bucharest-Magurele 077125, Romania*

(Received 6 February 2020; accepted 12 March 2021; published 2 April 2021)

Lifetimes of the low-energy levels in ^{136}Nd, populated in the reaction ^{124}Te(^{16}O, $4n$), were measured with the ROSPHERE array at the Horia Hulubei National Institute for Physics and Nuclear Engineering (IFIN-HH), Bucharest-Magurele. The data were analyzed using the recoil distance Doppler shift method, and, in the cases where lifetimes were $\tau \leqslant 1$ ps, Doppler attenuation effects were taken into account. The deduced electromagnetic transition probabilities are discussed in the framework of the five-dimensional collective Hamiltonian (5DCH) theoretical model implemented with the D1S Gogny force, and detailed systematics of several observables in the even-even Nd isotopic chain are presented that highlight the transitional character of the neutron-deficient Nd isotopes. The 5DCH predictions are in overall good agreement with the present experimental results.

DOI: 10.1103/PhysRevC.103.044306

I. INTRODUCTION

The ^{136}Nd nucleus lies in one of the two regions, centered on ^{140}Gd and ^{108}Ru, where the largest deviations from axial symmetry have been observed [1]. This has been a well-known fact for a long time, and several theoretical models have predicted triaxial ground state shapes based on modified harmonic oscillator [2], Woods-Saxon potential [3], or Hartree-Fock-Bogoliubov (HFB) calculations [4]. The neutron-deficient Ba and Xe nuclei can be described in terms of the occurrence of axial asymmetry, predominantly with a high degree of γ softness. For heavier nuclei, essential experimental data to draw valid conclusions are lacking, but the consensus is that the $N = 76$ nuclei are more γ rigid than the neighbors with higher neutron number [3,5].

In recent years the Nd isotopes have been studied intensively, and now there is proof that the lighter ^{132,134}Nd isotopes are much more γ soft than the heavier Nd neighbors [6,7]. We have shown in a previous investigation on ^{138}Nd that the low lying states have small deformation with softness in both β and γ degrees of freedom [8]. Also, evidence that supports the presence of shape coexistence between prolate and oblate shapes was found in the same study [8]. ^{140}Nd has been studied at the REX-ISOLDE facility, and the results agree with the general observation of spherical shapes near shell closure ($N = 82$) [9]. In the case of ^{136}Nd, the experimental information is rather scarce at low energies, especially concerning lifetime measurements. In the yrast band only the lifetime of the first 2^+ state obtained in two experiments—a Coulomb excitation experiment [10] and an recoil distance Doppler shift (RDDS) experiment [11]—were known, together with the upper limits for the 4^+ and 6^+ levels. Although recently several studies were performed, the aim was mostly centered on high spin states [12]. Also, evidence for chiral bands in even-even Nd nuclei has been pointed out [13]. These excited bands observed in ^{136,138}Nd have been interpreted within cranked self-consistent mean-field descriptions of rotating triaxial shapes [14,15]. The present work aims to add new information about collectivity at low energies in ^{136}Nd that will complete the picture of transition in Nd isotopes from deformed ($N \approx 70$) to spherical ($N \approx 80$) shape. The paper is organized as follows. Section II presents the experimental setup. Section III describes the recoil distance Doppler shift (RDDS) method, and Sec. IV the data analyses. These new experimental results together with earlier ones are analysed in Sec. V using a five-dimensional collective Hamiltonian (5DCH) based on the Gogny D1S force.

II. EXPERIMENTAL SETUP

The lifetime measurements of ^{136}Nd were performed at the Horia Hulubei National Institute for Physics and Nuclear Engineering (IFIN-HH) 9 MV Tandem Accelerator in Bucharest-Magurele. The ^{136}Nd nuclei were produced in

^{124}Te(^{16}O, $4n$) nuclear reactions using a target manufactured by the IFIN-HH target laboratory [16], consisting of ^{124}Te with 0.43 mg/cm^2 thickness deposited on a 3 mg/cm^2 gold backing. We used the CASCADE [17] and COMPA [18] codes to calculate the cross sections for producing ^{136}Nd. The cross section is ≈ 250 mb, for a projectile energy of 75 MeV and, for this reason, a beam of ^{16}O accelerated at 80 MeV was used to account for the energy loss in the gold backing facing the beam. The recoils had a velocity of 3.02 μm/ps ($v/c =$ 1.01%) and were stopped using a gold foil of 5 mg/cm^2. γ-γ coincidence measurements were performed to clean the spectra of unwanted γ rays resulting from other reaction channels and Coulomb excitation of the gold foils. As a reaction chamber, we used the Cologne-Bucharest Plunger Device known for its capacity to precisely adjust stopper-target distance. For γ ray detection, we used the ROSPHERE array [19] in its standard configuration of fourteen Compton-suppressed 55% high-purity germanium (HPGe) detectors placed on four rings at 37°, 70°, 90°, and 143° with respect to the beam direction, and eleven LaBr$_3$(Ce) scintilator detectors. Data were taken at 15 target-stopper distances ranging from 10 to 280 μm for an average of 24 h at shorter distances and 8 h at longer distances.

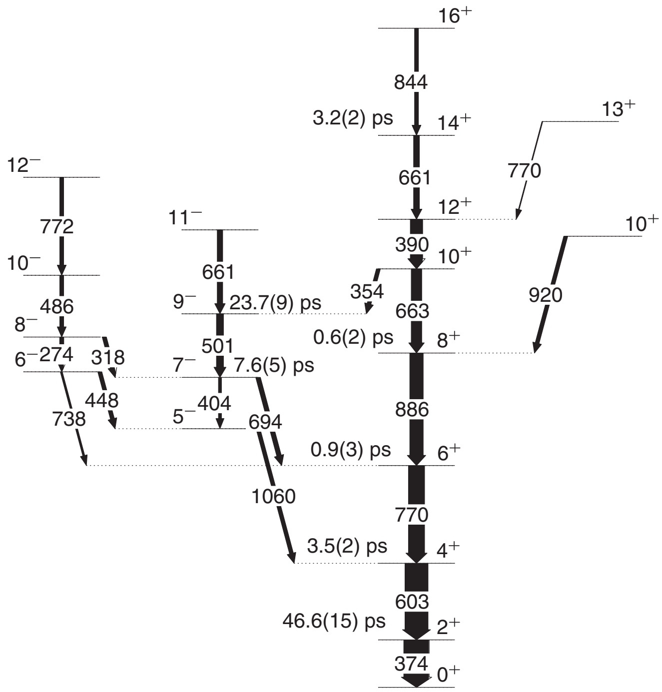

FIG. 1. Partial level scheme of ^{136}Nd that highlights the levels of interest for this experiment, constructed using observed intensities, and mean lifetimes measured in this experiment.

III. RDDS DATA ANALYSIS

The recoil dstance Doppler shift (RDDS) method is a well-established technique for the determination of picosecond lifetimes of excited nuclear states. A detailed presentation of the method can be found, e.g., in Ref. [20] and the newer review paper [21]. It is based on the time information that can be inferred from the splitting of the intensity of a depopulating γ-ray transition into components characterized by different Doppler shifts. Thus, emissions during the flight in vacuum lead to the detection of a γ ray with a Doppler-shifted energy contributing to a shifted (S) component in the spectrum. Emissions occurring at rest in the stopper contribute to an unshifted (U) component. When the distance between the target and stopper foils is varied, the ratio of the U and S peak intensities is also modified, ensuring sensitivity to the lifetime τ. Therefore, it is possible to deduce the lifetime of excited states by measuring spectra at different flight times between the foils. The precise determination of the areas of these two peaks at each distance is of crucial importance for the analysis of RDDS data.

In the present work, the differential decay curve method (DDCM) [21] was used to analyze the $2_1^+, 4_1^+, 7_1^-, 9_1^-$, and 14_1^+ states of ^{136}Nd, which allowed us to bypass the unobserved feeding problems of the RDDS method. The decay path, shown in Fig. 1, poses several issues caused by the overlap in the energy of some transitions that cannot be resolved with HPGe detectors. The $6^+ \rightarrow 4^+$ transition has an energy of 770.4 keV, the $13^+ \rightarrow 12^+$ transition has 769.7 keV, and the $12^- \rightarrow 10^-$ transition has 772.4 keV; therefore, gating on the shifted component of the $6^+ \rightarrow 4^+$ transition is impossible without gating on the shifted components of the other two transitions and, thus, contaminating the spectra.

Also, the lifetimes of the 12^+ state at 3686.6 keV and 10^+ state at 3278.6 keV are in the RDDS method sensitivity range, but, due to overlapping energies of the $14^+ \rightarrow 12^+$ and $10^+ \rightarrow 8^+$ transitions, we cannot extract their values.

For the DDCM analysis, the γ-γ coincidence events were sorted in a three-dimensional matrix that contains energies of the γ rays on two axes and the pair of detectors where γ rays were detected, on the third axis. By cutting this matrix with respect to the angle of detection we obtained three different matrices: forward-forward (37°, 37°), forward-backward (37°, 143°), and backward-backward (143°, 143°). From each of these matrices, we obtained a lifetime for each state we are interested in. The weighted average of these four values is the mean nuclear lifetime of the state. We took advantage of the γ rays emitted as a result of Coulomb excitation of the Au stopper and target backing to normalize the transition intensities in ^{136}Nd such as to account for the measurement time and beam intensity. Therefore, we gated on the 279-keV transition in ^{197}Au, and we used the sum of the 458- and 576-keV transition intensities as a normalizing factor. The recoil velocity was calculated using the energy of the shifted and unshifted components alongside the angle of detection, and we obtained a mean value for every matrix available.

In the coincidence measurements case, the lifetime τ at a distance x, in the DDCM framework while using a direct gate, is given by [21]

$$\tau(x) = \frac{\{B_S, A_U\}(x)}{\frac{d}{dx}\{B_S, A_S\}(x)} \frac{1}{v}, \tag{1}$$

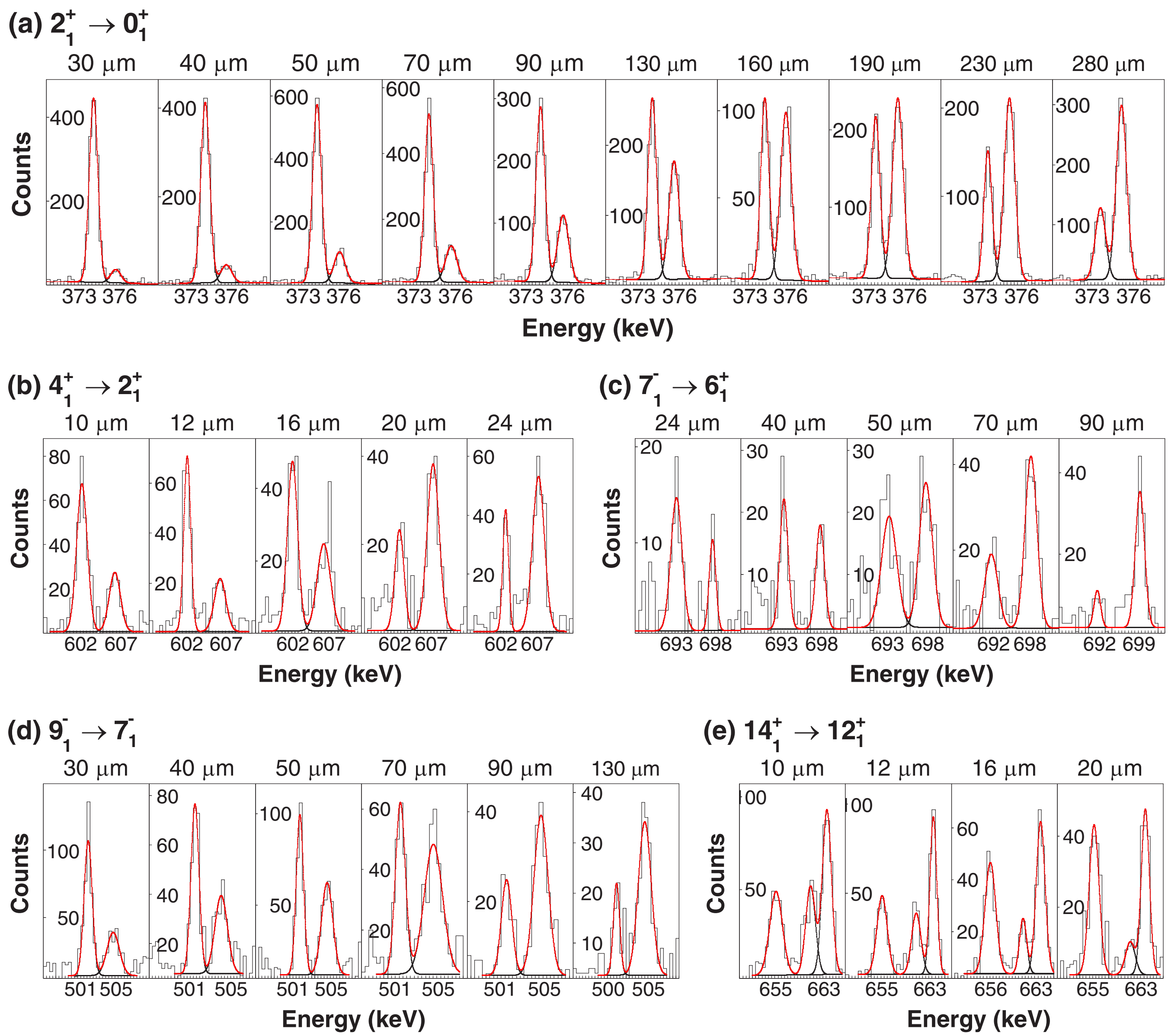

FIG. 2. Background subtracted spectra showing the peak intensity evolution of the S component and U component for $2_1^+ \rightarrow 0^+$ (a), $4_1^+ \rightarrow 2_1^+$ (b), $7_1^- \rightarrow 6_1^+$ (c), $9_1^- \rightarrow 7_1^-$ (d) transitions measured in the forward direction and $14_1^+ \rightarrow 12_1^+$ (e) in the backward direction. The transitions are obtained in coincidence with the S component of the feeding γ rays at 602.7, 886.0, 501.2, 661.2, and 844.3 keV, respectively.

where the quantities in brackets are the areas of the S peak and U peak of transition A while gated on the S peak of transition B. For the indirect gating case we have

$$\tau(x) = \frac{\{C_S, A_U\}(x) - \alpha\{C_S, B_U\}(x)}{\frac{d}{dx}\{C_S, A_S\}(x)} \frac{1}{v} \tag{2}$$

$$\alpha = \frac{\{C_S, A_U\}(x) + \{C_S, A_S\}(x)}{\{C_S, B_U\}(x) + \{C_S, B_S\}(x)}, \tag{3}$$

where the quantities in brackets are the areas of the S peak and U peak of transitions A and B while gated on the S peak of transition C in a C-B-A cascade.

A. The 2^+, 4^+, 7^-, 9^- and 14^+, states

In the case of the $I^\pi = 2^+$ state at 373.7 keV, a gate was placed on the Doppler shifted component of the $4^+ \rightarrow 2^+$ transition and both areas of the S and U components of the $2^+ \rightarrow 0^+$ transition were determined. The intensity evolution of the 373-keV γ ray measured at ten different distances in the forward direction is presented in Fig. 2(a). The lifetime analysis is shown in Figs. 3(a) and 3(b). In the lower panel, the intensity of the "shifted" (red) and "unshifted" (black) components are represented as a function of target-to-stopper distance in the sensitivity region. The data are fitted using two continuously differentiable second-degree polynomials such that the polynomials fit the S component and their derivatives

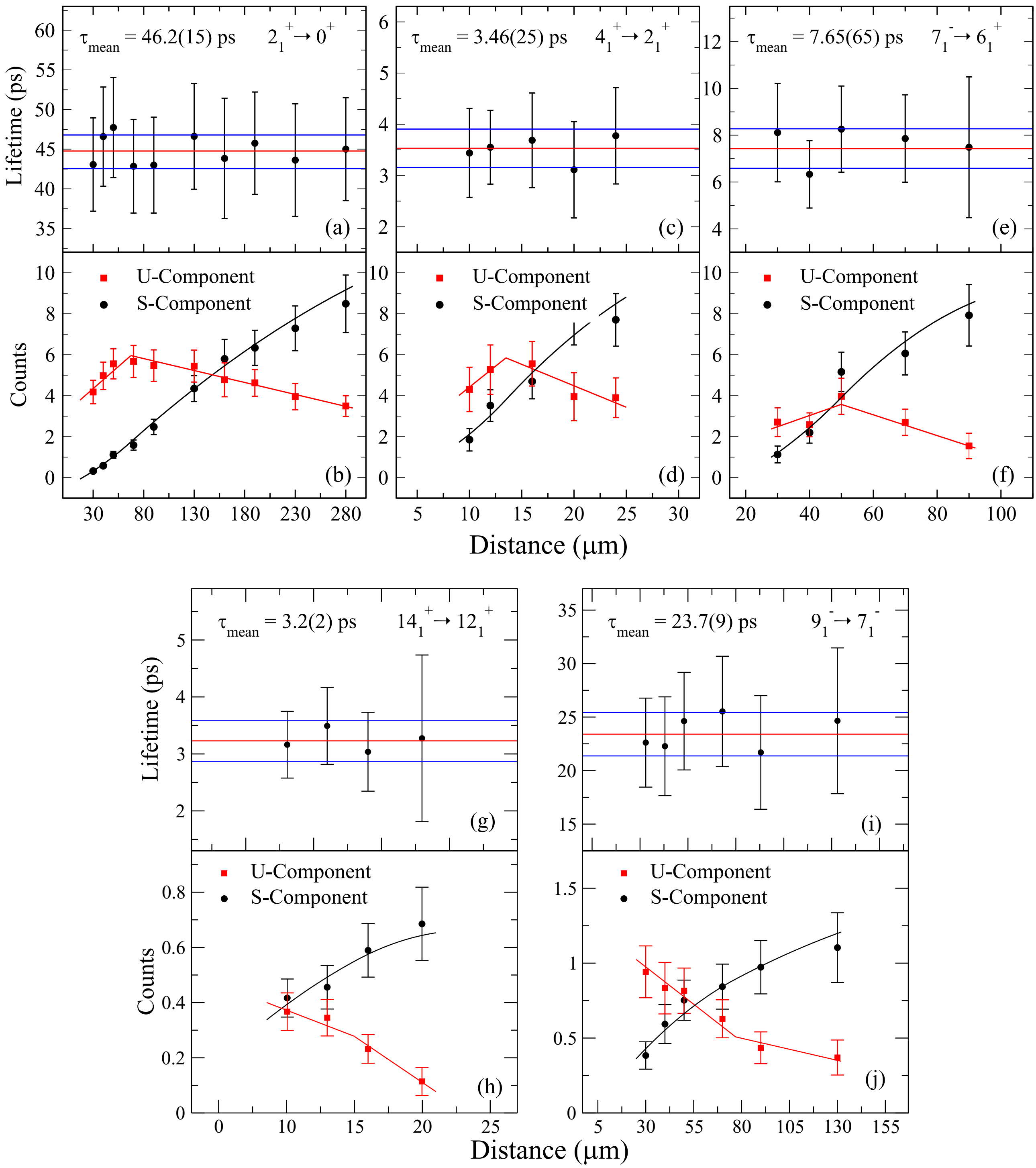

FIG. 3. Mean lifetimes for the 2_1^+ (a), 4_1^+ (c), 7_1^- (e), 9_1^- (i) states for each distance measured in the forward direction (37°) and for the 14_1^+ (g) state measured in the backward direction (143°). The horizontal lines are the weighted averages of these values and their uncertainties. Normalized values of the S component (black circles) and U component (red squares) of the $2_1^+ \rightarrow 0^+$ (b), $4_1^+ \rightarrow 2_1^+$ (d), $7_1^- \rightarrow 6_1^+$ (f), $9_1^- \rightarrow 7_1^-$ (j) transition intensities measured in the forward direction and of the $14_1^+ \rightarrow 12_1^+$ (h) transition intensity measured in the backward direction.

fit the U component. Figure 3(a) shows the lifetime obtained at each distance measured, calculated using Eq. (1) and the polynomials from Fig. 3(b). The weighted average of these values represents the mean lifetime of the 2^+ state obtained in the forward-forward matrices, and, alongside the values obtained from the backward-backward and forward-backward matrices, we deduced the final lifetime for the 2^+ state as 46.2(15) ps. The value obtained is summarised alongside all other lifetimes in Table I. The reduced transition probabilities $B(E2)$ deduced from this measurement are also summarized

TABLE I. Lifetimes measured in the present work. The reduced transition probabilities obtained in the present work and the theoretical values calculated using 5DCH calculations are alongside the previously known values.

E_x (keV)	J_n^π	E_γ (keV)	α[a]	Gate	τ (ps)	$B(E2)$ (W.u.) previous	$B(E2)$ (W.u.) present	$B(E2)$ (W.u.) theoretical
373.75	2_1^+	373.7	0.0268	$4_1^+ \rightarrow 2_1^+$	46.2(15)	80(11)[b]	56.8(19)	57
976.46	4_1^+	602.7	0.00723	$6_1^+ \rightarrow 4_1^+$	3.46(25)	>21[c]	71(5)	92
1746.80	6_1^+	770.4	0.00400	$8_1^+ \rightarrow 6_1^+$	0.93(25)	>3[c]	78(21)	123
2439.80	7_1^-	404.1	0.0213	$9_1^- \rightarrow 7_1^-$	7.65(65)	14(5)[c]	54(5)[d]	
2632.80	8_1^+	886.0	0.00291	$10_1^+ \rightarrow 8_1^+$	0.6(2)	>3.5[c]	59(20)	156
2941.0	9_1^-	501.2	0.01170	$11_1^- \rightarrow 9_1^-$	23.75(92)	71(24)[c]	25.9(10)	
4347.8	14_1^+	661.3	0.00574	$16_1^+ \rightarrow 14_1^+$	3.14(27)	>27[c]	49(5)	

[a]Conversion coefficient values taken from [6].
[b]jugal $B(E2)$ value taken from [10].
[c]jugal $B(E2)$ values taken from [22].
[d]Branching ratio used to calculate the B(E2) value, $I_{404.1} = 22.7\%$, taken from [36].

in Table I. The total uncertainty was given by the statistical uncertainties arising from the fit, the error in measuring the recoil velocity, and the fluctuations of the distance throughout the experiment.

For the $I^\pi = 4^+$ state at 976.5 keV, gating on the transition that directly feeds the level was not possible because of contaminations. Therefore, we have used an indirect gate on the S peak of the $8^+ \rightarrow 6^+$ transition. With this gate, we bypass the contaminants coming from the negative parity band, as can be seen in Fig. 1, and, because the 13^+ level at 4454.6 keV was weakly populated, we minimized the contamination. The data analysis was almost the same as in the case of the 2^+ state, the only difference being that we had to take into account the S peak and U peak for the transitions that directly feed the level ($6^+ \rightarrow 4^+$) and the one through which it decays ($4^+ \rightarrow 2^+$). The mean lifetime for the 4_1^+ state obtained after the analysis is 3.46(25) ps.

The mean lifetime for the $I^\pi = 7^-$ state at 2439.8 keV could also be extracted using the DDCM method. For this level, we gated on the S component of the 501-keV transition from the 9^- level, and we measured the 694-keV transition through which the level decays to the 6^+ state. For this level, we obtained the mean lifetime of 7.65(65) ps.

For the $I^\pi = 9^-$ state at 2941.0 keV, we used a gate on the S component of the 661-keV transition that feeds the level and we measured the intensity of the 501-keV transition that depopulates the level. For this level we obtained the mean lifetime of 23.75(92) ps.

The negative parity states were previously measured using the singles RDDS method [22]. They obtained for the 9^- states a lifetime of 9(3) ps and for the 7^- state 31(10) ps, as compared with 23.75(92) and 7.65(65) ps values obtained for the 9^- and 7^-, respectively, in the present study. A close inspection of these values indicates that the interchanged values from [22] are in good agreement with our measurements. It is well known that the singles RDDS method may lead to inaccurate results if the feeding times are not correctly identified [21]. Therefore, it is possible that, after solving the differential equations, the lifetimes were correctly measured but improperly assigned.

The last state that we could measure in this experiment is the $I^\pi = 14^+$ state at 4347.8 keV. In this case, we gated on the S component of 844-kev transition and we measured the intensity of the 661-keV transition to the $I^\pi = 12^+$ state. The mean lifetime obtained for the 14_1^+ state is 3.14(27) ps.

IV. RDDS ANALYSIS WITH DSAM EFFECTS

The methods employed for the analysis of the 6^+ and 8^+ levels ($\tau \leqslant 1$ ps) require a Monte Carlo (MC) simulation of the time evolution of the velocity distribution of recoils by describing the processes of creation, slowing-down in the target, free flight in vacuum, and slowing-down in the stopper of the recoil nuclei. The "velocity histories" are additionally randomized with respect to the registering detectors. We used a modified version of the computer code DESASTOP [23–25] for the Monte-Carlo simulation. To take into account the reduction of the beam energy when passing through the target foil, we used reaction cross sections calculated with the code CASCADE [17]. The electron stopping power $(\frac{d\epsilon}{d\rho})_e$ was derived according to the procedure outlined in Ref. [25] from the semiempirical tables of Northcliffe and Schilling [26] taking into account the effects of the medium atomic structure [27,28]. It is treated numerically above a specific energy limit. Below this limit, we used a formula which generalizes the theory [29] of Lindhard, Scharff, and Schiøtt (LSS) [30]. In the corresponding dimensionless units, it states

$$\left(\frac{d\epsilon}{d\rho}\right)_e = f_e k_{LSS} \epsilon^a, \tag{4}$$

where k_{LSS} is a constant given by theory.

For the ^{136}Nd ions in the ^{122}Te target, we used the parameters $f_e = 0.832$ and $a = 0.594$, while, for the gold stopper, the values were $f_e = 0.511$ and $a = 0.631$. These parameters were obtained by fitting the electron stopping powers with the function presented in Eq. (4). The reduction factor f_n of the nuclear stopping power was treated as an adjustable parameter, and a value of 0.7 was adopted as suggested in Refs. [28,31]. The factor f_n scales down the cross section for nuclear scattering in the Monte Carlo procedure. At large distances, the line shapes of the shifted peaks were well reproduced, which we consider an indication that the stopping powers of the target material were correctly taken into account. The simulation predicts that almost all recoils leave the target with a mean v/c of 1.05%, and the slowing down in the stopper takes place in a mean time of 0.83 ps, while all recoils are fully stopped within 1.4 ps.

A. The 6^+ state

In the case of the $I^\pi = 6^+$ level, we used gates from below (GFB). It was found that a gate set on the whole line shape (shifted and unshifted components included) of the transition of 602.7 keV depopulating the 4^+ level was suitable for further analysis. This approach does not solve the problem of the unknown (unobserved) feeding, but the intensity balance at the $I^\pi = 6^+$ level revealed that this feeding is less than 12%. The presence of possible deorientation effects was investigated by observing the behavior of the sum of the shifted and unshifted components as a function of the target-to-stopper distance. Within the error bars, no deviation from constant behavior was found, and the conclusion was drawn that the present results are not affected by the deorientation. Below we briefly review the main steps of the analysing procedure, directing the reader to Ref. [32] for more details. In the analysis procedure, the background-subtracted line shapes corresponding to the transition of interest at all distances and the decay curve of the shifted component,

$$S_{ij}(t) = b_{ij} \int_0^t \lambda_i n_i(t')dt', \tag{5}$$

are fitted simultaneously. The "unshifted" decay curve is given by the complementary integral

$$R_{ij}(t) = b_{ij} \int_t^\infty \lambda_i n_i(t')dt' = S_{ij}(\infty) - S_{ij}(t). \tag{6}$$

In Eqs. (5) and (6), $n_i(t)$ is the population of the level of interest i as a function of time, λ_i is its decay constant (the lifetime $\tau_i = 1/\lambda_i$), and b_{ij} is the branching ratio of the transition $i \to j$. The function $S_{ij}(t)$ is represented by second-order polynomials continuously interconnected at the borders of an arbitrarily chosen set of neighboring time intervals. The fitting procedure consists of changing the borders of the time intervals until the best reproduction of the spectra is achieved.

For singles-like RDDS measurements, also when the gates used do not involve a time dependence, the expression for the lifetime of the level of interest τ_i at every distance x or flight time $t = x/v_z$ provided by the DDCM [33] reads

$$\tau_i(t) = \frac{R_{ij}(t) - b_{ij}\sum_{k=1}^{N}(1+\alpha_{ki})R_{ki}(t)}{b_{ij}\lambda_i n_i(t)}. \tag{7}$$

The numerator gives the number of nuclei $n_i(t)$ at time t which decay via the transition $i \to j$. The quantities α_{ki} are the internal conversion coefficients of the directly feeding γ-ray transitions $k \to i$. The denominator represents the first derivative of the decay curve of the shifted component $S_{ij}(t)$ or the decay function of the transition $i \to j$. In Ref. [32], it was shown that taking into account the velocity distribution and Doppler-shift attenuated (DSA) effects leads to the following equation for each distance x or mean end-of-flight time $\langle t_{f_f}\rangle$:

$$\tau(t) = \frac{\tilde{R}_{ij}(x) - b_{ij}\sum_{k=1}^{N}(1+\alpha_{ki})\frac{I^\gamma_{ki}\tilde{S}_{ij}(\infty)}{I^\gamma_{ij}\tilde{S}_{ki}(\infty)}\tilde{R}_{ki}(x)}{\frac{d\tilde{S}_{ij}}{dt}\big|_{t=t_s}}. \tag{8}$$

Here, the quantities I^γ are the relative intensities of the γ-ray transitions and $\tilde{S}(\infty)$ are the values of the fitted decay curves of the shifted components at long times (i.e., when they reach constant values). The γ-ray intensities have to be known independently. In the present case, we have determined them using a careful efficiency calibration. The quantities $\tilde{R}$ are the areas of the corresponding unshifted peaks. The denominator in Eq. (8) represents the derivative $d\tilde{S}_{ij}(t)/dt$ taken at the stop-time t_s and averaged over the MC histories used for the fits of the RDDS spectra and $\tilde{S}_{ij}(t)$. The final result for the lifetime for a particular ring combination is obtained by fitting a straight line through the points calculated according to Eq. (8) (the τ curve) within the region of sensitivity. Deviations of the τ curve from a constant indicate systematic errors in the analysis and give feedback for improvements.

Figure 4 shows the analysis of the data for the 770.4 keV transition which depopulates the $I^\pi = 6_1^+$ level of the yrast band. In the analysis, the three direct feeding transitions of that level were included, namely those of 886.9, 693.1, and 737.1 keV. It was found that, in the reaction used, the even-spin negative parity sequence of levels starting at the 6^- level at 2483.8 keV is much less populated than the odd-spin one, and therefore the transition of 772.4 keV in the even-spin sequence does not disturb significantly the lifetime determination as a contaminant. However, a contaminant was found at a γ-ray energy of 766.7 keV, which very quickly decays and displays an unshifted component only at the smallest few distances. This contaminant could not be assigned to a particular nucleus observed in the reaction. We simulated line shapes at various distances for this transition which reproduce the corresponding part of the γ-ray spectra. These simulated line shapes were subtracted from the experimental spectra obtained by gating on the $4_1^+ \to 2_1^+$ transition of 603 keV. The resulting spectra were analyzed as described above and as illustrated in Fig. 4. Averaging the results for the lifetime derived at the forward and backward angles indicated in Fig. 4 leads to the lifetime $\tau = 0.93$ (25) ps.

B. The 8^+ state

In the case of the $I^\pi = 8^+$ level, the RDDS data were analyzed according to the procedure from Ref. [23], which represents a further extension of DDCM [33,34]. This technique takes into account the velocity distribution of the recoils and the finite slowing-down time in the stopper. We are referring the reader to the above works for more details as we will only present the main points.

The emissions of γ rays by the recoiling nucleus in the target, during its free flight in vacuum and the slowing down in the stopper, as well as while at rest in the stopper, are distinguished in this approach. Thus, the Doppler-shifted γ-ray spectra generated by emissions occurring during the flight in vacuum (SF) and slowing-down in the stopper (SS) can be described. The detector response function is used to describe

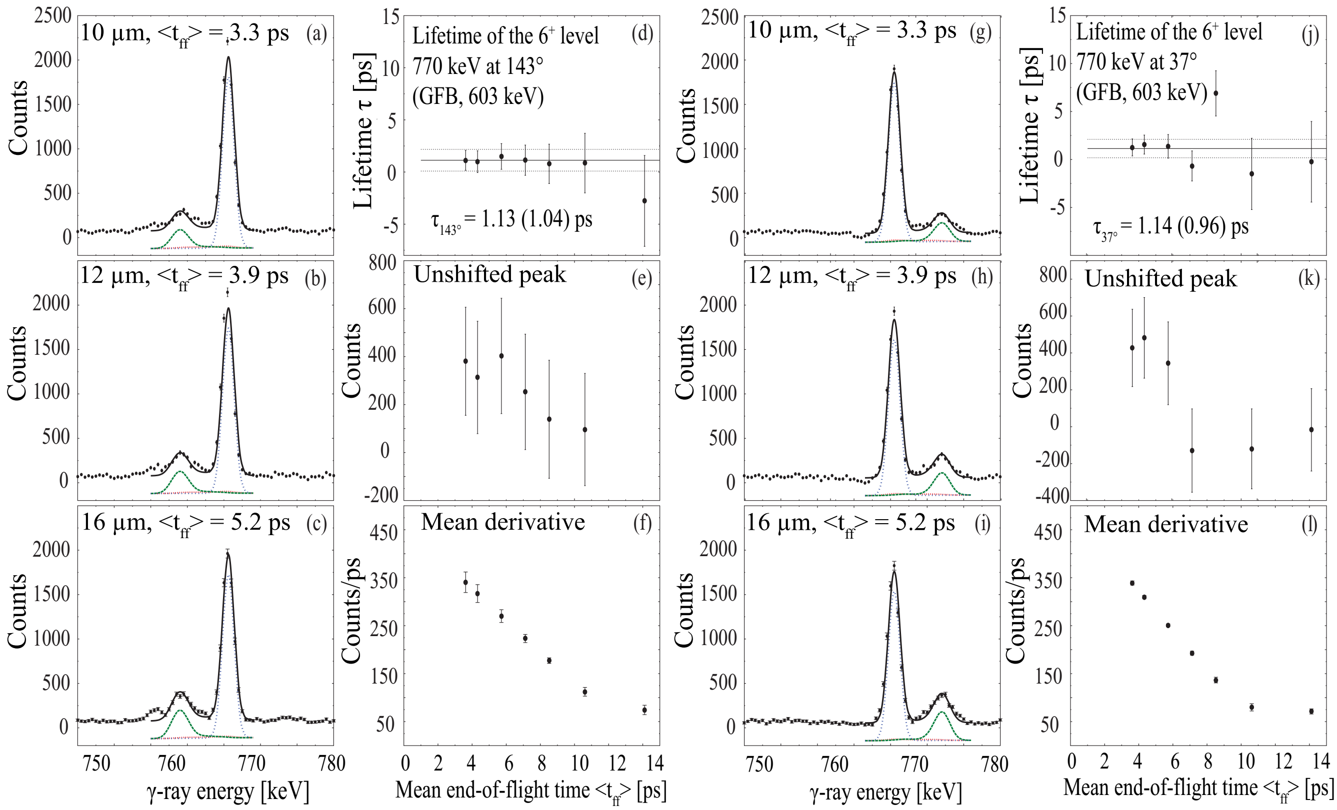

FIG. 4. Lifetime determination for the 6_1^+ level in the yrast band of ^{136}Nd using the gated spectra measured with the detectors at 143° (left two groups of panels) and 37° (right two groups of panels). The gate is set on the full line shape of the γ-ray transition of 603 keV on the bottom of the band (GFB). The first and third groups of panels present fits of the line shape of the 770 keV γ-ray transition at different distances. The solid black line is the full fit. The decomposition of the line shape into different components is also shown, with a subtracted constant and common number from the calculated spectra for more visibility. Namely, these are the unshifted peak and background (dashed blue line), the spectrum part generated by DSA effects (dotted red line), and the pure flight peak represented by a green long-dashed line. The second and fourth groups of panels illustrate the lifetime determination according to Eq. (8). On top, the derived τ curve is displayed with its uncertainties together with a fit with a horizontal line derived within the region of sensitivity. This curve is a result of the division of the numerator in that equation (middle panel) by the corresponding denominator (bottom panel). The mean lifetimes determined and their uncertainties are also shown. See also the main text.

the unshifted peak (U) originating from emissions at rest. The different combinations of the emission times of the transition feeding the level of interest (denoted by B) and of the transition which depopulates this level (denoted by A) yield separate contributions to the RDDS spectra obtained by setting a gate on any part of the "shifted" component of the transition B. These contributions are disentangled by a fitting procedure whose details are given in Ref. [23]. At each distance x or mean end-of-flight time $\langle t_{f_f}\rangle$, the lifetime τ of the level of interest is derived using the following expression [23]:

$$\tau(x) = \frac{(\{B_{SF}, A_U\} + \{B_{SS}, A_U\})}{\left\langle\frac{d(\{B_{SF},A_{SF}\}+\{B_{SF},A_{SS}\}+\{B_{SS},A_{SS}\}}{dt_{f_f}}\right\rangle}, \tag{9}$$

where the quantities in braces are the areas of the corresponding contributions to the full gated spectrum. For the particular combination of "gating" and "gated" detector rings considered, the lifetime is derived by fitting a horizontal line through the points of this $\tau(x)$ curve within the region of sensitivity where the numerator and denominator in Eq. (9) are reliable. The final value is determined by averaging the results obtained using all analyzed two-ring combinations. We note that the additional corrections of the data for relativistic, efficiency, and solid angle effects can be neglected in the present analysis. The deorientation effect was shown to not affect the results of the analysis of coincidence RDDS measurements when it is performed in the framework of the DDCM with a gate on the shifted component of a feeding transition [35].

For the 8^+ level in ^{136}Nd, gates were set on the shifted component of the γ ray of 919.7 keV which directly feeds that level by its decay from the $I^\pi = 10^+$ level at 3556.2 keV. Only the backward ring detectors were used for gating to avoid contaminants. The lifetime analysis including the fitting of the line shapes and the lifetime determination is shown in Fig. 5, where the Doppler-shift attenuated (DSA) fraction due to emissions during the slowing down is also displayed. The averaged value from the analysis at the backward and forward rings points to a lifetime $\tau = 0.6$ (2) ps.

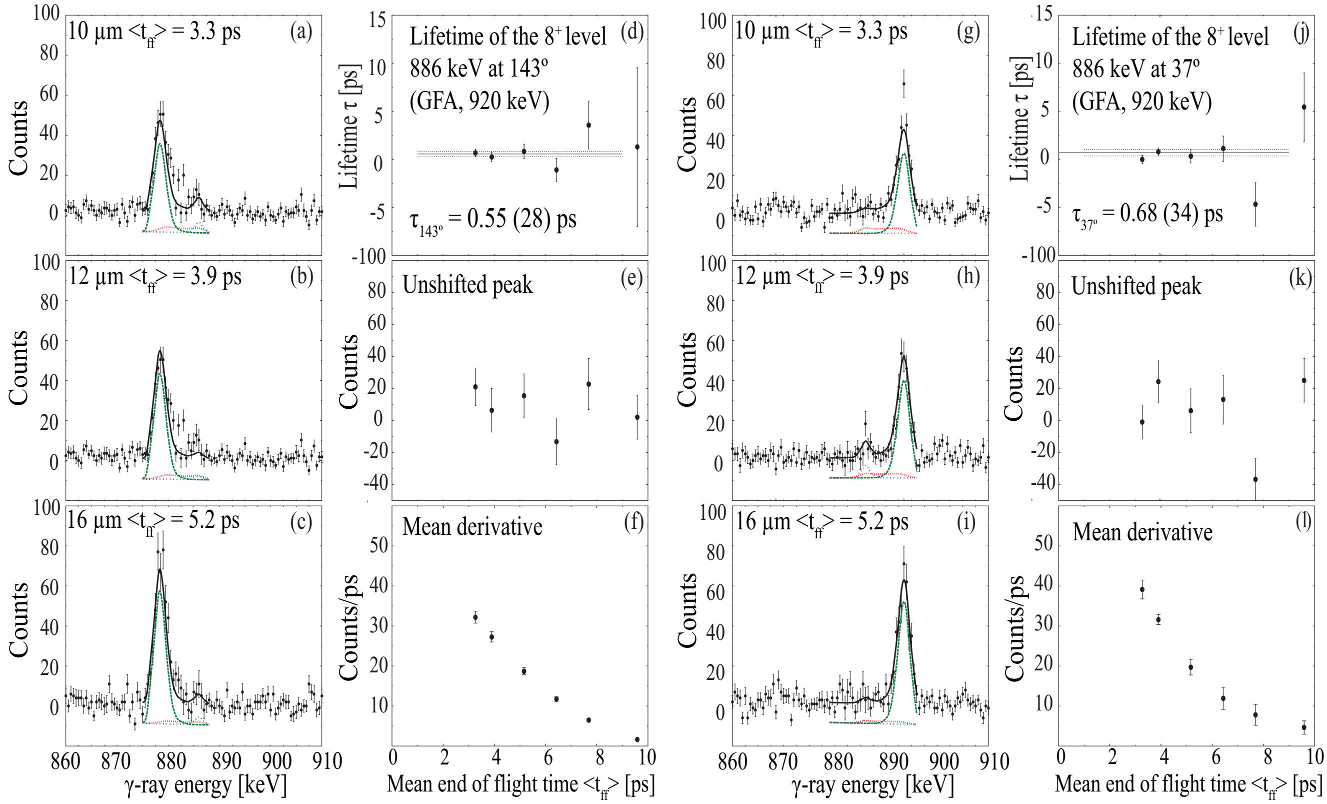

FIG. 5. Lifetime determination for the 8_1^+ level in the yrast band of ^{136}Nd using the gated spectra measured with the detectors at 143° (left two groups of panels) and 37° (right two groups of panels). The gate is set on the shifted component of the directly feeding transition of 920 keV observed with the detectors of the backward ring. The first and third groups of panels present fits of the line shape of the 886 keV γ-ray transition at different distances. The solid black line is the full fit. The second and fourth groups of panels illustrate the lifetime determination according to Eq. (9). On top, the derived τ curve is displayed together with a fit with a horizontal line derived within the region of sensitivity. See also the caption to Fig. 4 and the text.

C. Discussion on the 2_1^+ state lifetime

Previously, the lifetime of the first 2^+ state in ^{136}Nd was measured in two experiments. In the first one, the first 2^+ state was populated by Coulomb excitation at relativistic energies [10]. Using the FRS-RISING setup at GSI, Darmstadt [37], they measured the reduced transition probability $B(E2)$ to be 80(11) W.u., that translates to a mean lifetime of 34 (7) ps. The second experiment was a recent RDDS experiment [11] using the EAGLE array [38] and the U-200P cyclotron at the Heavy Ion Laboratory in Warsaw. Their aim was to measure the lifetime of the 10^+ isomeric state at 3278.7 keV, populated in the ^{120}Sn(^{40}Ne, $4n$)^{136}Nd reaction, using the RDDS technique. Since the goal was to measure a lifetime in the ns region, the authors measured at 13 distances between 74 μm and 5 mm. However, the lifetimes for the 2^+ state at 373.7 keV and the 12^+ state at 3686.4 keV are in the sensitivity range. The authors used five distances between 90 and 160 μm and obtained for the 2_1^+ state a mean lifetime of 38(2) ps. Both values for the lifetime of the first 2^+ level, obtained in independent experiments, are in agreement with each other but are in contradiction with the present result of 46.2(15) ps. Considering this situation, we are compelled to bring more evidence to support our result. As we have mentioned before, the ROSPHERE was equipped with eleven $LaBr_3$(Ce) detectors, so we were able to extract the lifetime of the first 2^+ state using also the in-beam fast-timing method.

The method takes advantage of the fast timing response (≈200–300 ps) and the good energy resolution (3–4%) of the $LaBr_3$(Ce) detectors and of the excellent energy resolution (≈0.15%) of the HPGe detectors [19]. By employing a triple-γ coincidence condition [one HPGe AND two $LaBr_3$(Ce)] for the high multiplicity nuclear reaction (e.g., fusion evaporation), one can gate using the HPGe detectors to enhance the peak intensities of the γ rays that feed and deexcite the level of interest in the $LaBr_3$(Ce) detectors' spectra. From the time difference between the two γ rays observed in the $LaBr_3$(Ce) detectors, a time spectrum is constructed. The lifetime is extracted by one of the following methods: centroid shift, deconvolution, or slope method, depending on the value of the lifetime with respect to the FWHM of the prompt response curve of the setup. More details about the method and the procedure for extracting the lifetimes can be found in Ref. [39].

The $LaBr_3$(Ce) energy spectra were calibrated and the time-energy effect was corrected employing a ^{152}Eu source. Only full energy peaks were used for the time-walk correction and the result was validated against the lifetimes of the 4_1^+ and 6_1^+ states obtained in the present paper via the RDDS measurements. For the 4_1^+ state a lifetime of 3(6) ps and for the 6_1^+ state a lifetime of 4(6) ps were obtained with the fast-timing method. A run-by-run energy spectra calibration of the $LaBr_3$(Ce) detectors was performed using a gain correction algorithm [40] for the analysis of the experimental data.

Gates on the 501-, 663-, 693-, 770-, and 886-keV γ rays were set in the HPGe detectors to emphasise the known γ rays that feed and deexcite the 2_1^+ state. Then, $E_{\gamma_1}E_{\gamma_2}\Delta T$ matrices for the γ rays detected in the $LaBr_3$(Ce) detectors were created for each of the gates set on γ lines in the HPGe spectra and also for gates corresponding to the background of each of them. The quantity ΔT represents the time difference between the detection times of the two γ rays.

Careful gating on the $LaBr_3$(Ce) detectors was needed in order to exclude contributions from the 354- and 390-keV γ rays. Two areas with a size of 22 keV around these energies were avoided when selecting the 603-374 keV coincidence.

The time delayed spectra were extracted from the $E_{\gamma_1}E_{\gamma_2}\Delta T$ matrices using two-dimensional conditions on the energy. Two time spectra were produced from each matrix, one corresponding to the coincidence of the two γ rays and the other one to the background. The latter was subtracted from the former proportional to the ratio of the areas of each two-dimensional condition used to obtain them. Applying this method, the Compton contribution in the $LaBr_3$(Ce) detectors spectra was subtracted.

A second Compton contribution that comes from the HPGe detectors had to be removed in the present analysis. For this purpose, the matrices obtained by gating on the background in the HPGe detectors were analyzed using the same procedure as for the full energy ones. Each background time spectrum was subtracted from the corresponding time spectra of the full energy gate in the HPGe detectors proportional to the width of the gates.

Using the centroid shift method, a lifetime was extracted for the 2_1^+ state for each pair of gates used on the HPGe detectors. The same operations were also performed by reversing the feeding with the deexciting γ ray when cutting with the two-dimensional conditions. The antidelayed timing information was then extracted. By cross-checking these values we concluded that we do not have contaminants that contribute to the lifetime of the 2_1^+ state and proceeded to sort a $E_{\gamma_1}E_{\gamma_2}\Delta T$ matrix where all the full energy HPGe gates were used and one matrix for the background gates.

In Fig. 6, the time delayed spectra for the 2_1^+ state are presented. The adopted value of 51(6) ps for the lifetime of the 2_1^+ state is a mean value of the lifetimes obtained from the the delayed and antidelayed time spectra using both the centroid shift and deconvolution [41] methods. The uncertainty of the result reflects the statistical uncertainty and the systematic uncertainty which also accounts for the time-walk difference for the start and stop energies.

To summarize, the lifetime obtained with the fast-timing method [$\tau = 51(6)$ ps] has a larger uncertainty but is in agreement with the one obtained in this paper using the RDDS technique [$\tau = 46.2(15)$ ps]. The fast-timing method was proven several times to give reliable results even for shorter lifetimes [39,42,43]. In addition, the value from the RDDS measurement was obtained using ten distances that cover almost the entire sensitive region. As the lifetime for the 2_1^+ state was extracted with two independent methods, we believe the present RDDS measurement provides a reliable result.

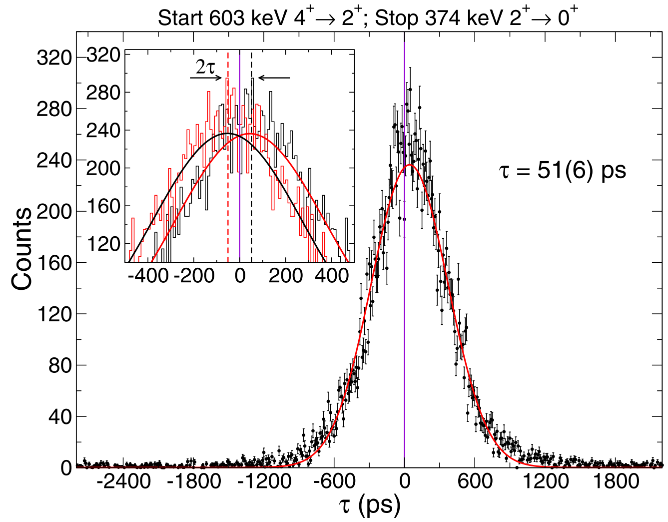

FIG. 6. Time delayed spectra corresponding to the lifetime of the 2_1^+ state. The continuous line represents the convolution of the prompt response and the lifetime of the state. In the inset, the time difference between the centroids of the delayed (black histogram and red line) and the antidelayed (red histogram and black line) time distributions is shown.

V. THEORETICAL INTERPRETATION

In order to get a better understanding of the transition phenomena occurring in this region we performed theoretical calculations of all even-even neutron-deficient Nd isotopes. The present studies rely on configuration mixing calculations [44] based on constrained Hartree-Fock-Bogoliubov (CHFB) calculations implemented using the D1S Gogny force [45,46] and performed by expanding solutions on a harmonic oscillator basis which includes eleven major shells. Potential energy surfaces (PESs), zero-point energies, and tensors of inertia are obtained as building blocks of a five-dimensional collective Hamiltonian (5DCH) that is solved as described in [47].

A. Potential energy surfaces

The neutron-deficient neodymium isotopes $^{130-140}$Nd display a transitional character, with PESs showing an evolution from well deformed (^{130}Nd) to spherical shape (^{140}Nd), with triaxial shallow minima for $^{134-138}$Nd. The PESs are shown in Fig. 7 over β and γ, the triaxial coordinates defined from mean values taken by mass quadrupole operators in the constrained HFB calculations [44,47]. The shape evolution taking place through the Nd isotopes is best defined using $\langle\beta\rangle$ and $\langle\gamma\rangle$ as mean deformations of the 5DCH solutions. For the ground levels and ground-state (gs) bands with angular momentum I, $I = 0$ to $8\hbar$, the mean deformations display triaxial trajectories. All isotopes show increasing deformations with increasing I, as shown in Fig. 8 where it is seen that a near maximum triaxial character, with $25^\circ < \langle\gamma\rangle < 30^\circ$ is reached for the isotopes $^{134-138}$Nd.

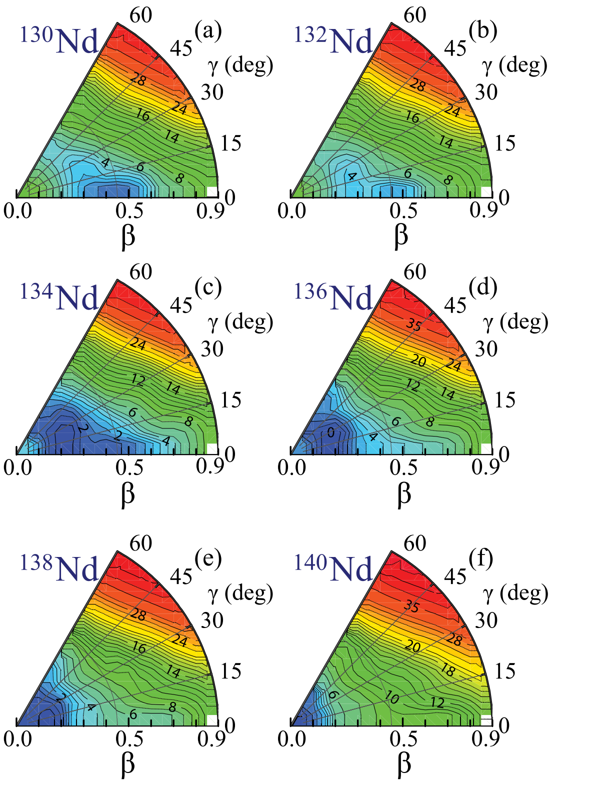

FIG. 7. Potential energy surfaces (MeV) over the (β, γ) collective coordinates for even-even mass Nd isotopes with neutron numbers from $N = 70$ to $N = 80$.

B. Ground state bands: Level schemes

In Fig. 9 are shown experimental gs level sequences (red circles) [48–53], for $N = 70$ to $N = 80$, which are compared up to $I = 8\hbar$ with those from 5DCH calculations (black circles). The data and calculations are in reasonable agreement for the lighter ^{130,132,134}Nd isotopes. The agreement gets worse for $N = 78$–80, that is in the vicinity the $N = 82$ shell closure. The 5DCH theory best describes nuclei away from shell closures.

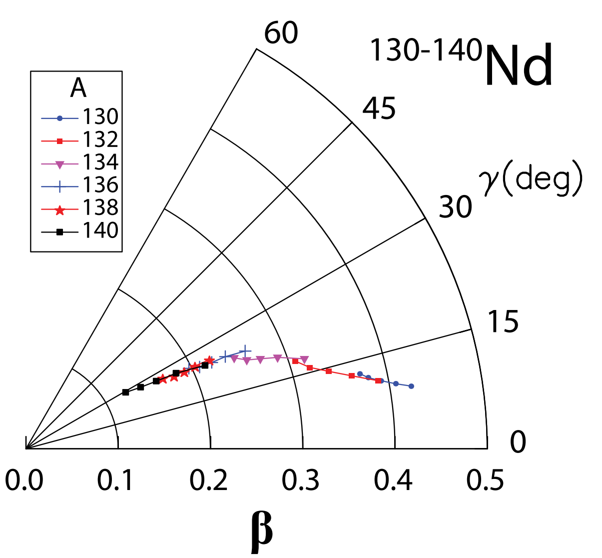

FIG. 8. Mean β and γ deformations of Nd ground state levels over the (β, γ) plane. Mean deformations calculated for spin values up to $I = 8$ form trajectories shown as continuous lines. The color code is intended to identify each trajectory.

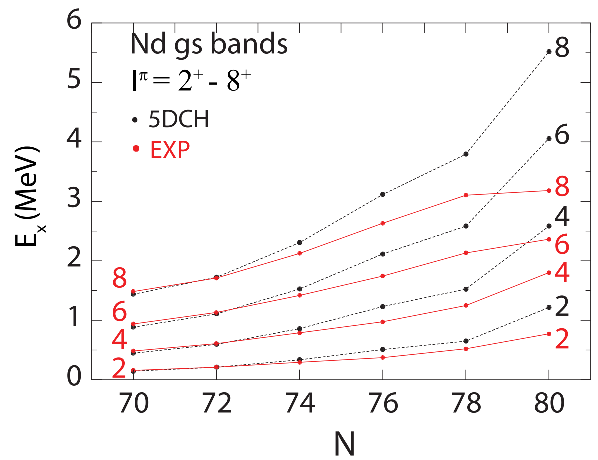

FIG. 9. Excitation energies (MeV) of ground state band levels up to spin $I = 8\hbar$. The red and black circles are for experimental [48–53] and calculated values, respectively.

C. Moments of inertia of yrast bands

To further explore the collective model predictions, 5DCH calculations have been extended to higher spins, $I < 18\hbar$, to determine kinetic moments of inertia, $\mathcal{J}^{(1)}$, of yrast bands as functions of rotational frequency ω. The $\mathcal{J}^{(1)}$ values, which provide measures of deformations conveyed by rotational bands, are shown as continuous curves in Fig. 10 using distinct symbols for each isotope. In order to trace the structure evolution taking place through the neutron-deficient Nd isotopes, calculations have been conducted for $N = 64$–80, with $N = 64$ the neutron number close to that for the proton drip line. As can be seen in Fig. 10(i) the isotopes with $N = 64$ to 68 show smoothly increasing $\mathcal{J}^{(1)}$ values, and (ii) those

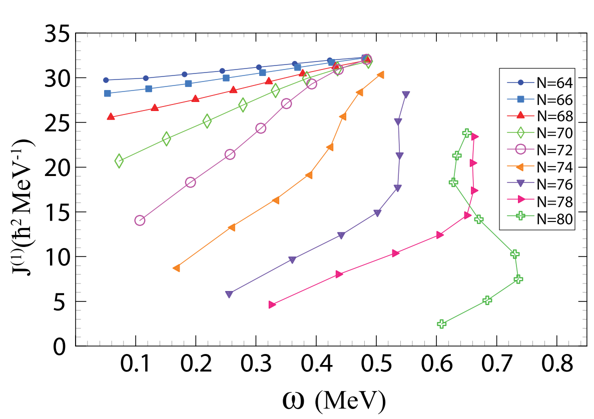

FIG. 10. Calculated $\mathcal{J}^{(1)}$ values ($\hbar^2$MeV^{-1}) for yrast bands in Nd isotopes with neutron numbers $N = 64$ to $N = 80$. For details see text.

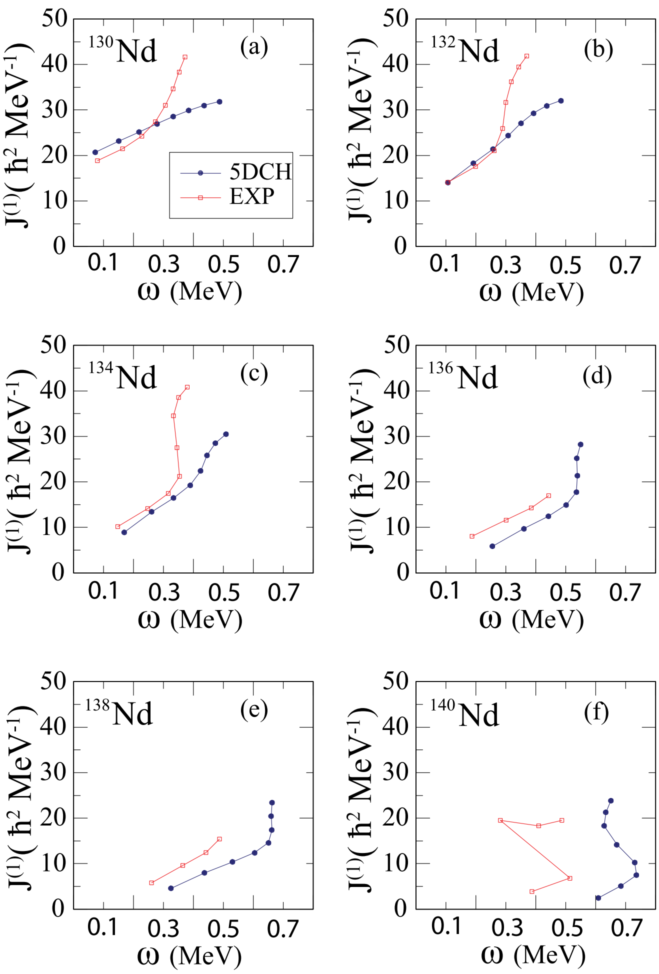

FIG. 11. Kinetic moments of inertia $\mathcal{J}^{(1)}$ ($\hbar^2$MeV^{-1}) of ground state bands for the $^{130\text{–}140}$Nd isotopes, as functions of rotational frequency ω (MeV). The red and blue symbols connected by continuous lines are for experimental [48–53] and calculated values, respectively. For convenience experimental data for ^{136,138}Nd are not shown at frequency $\omega > 0.5$ MeV.

with $N = 70$ to 74 display $\mathcal{J}^{(1)}$'s starting to bend at high frequencies. Up-bending is established in $\mathcal{J}^{(1)}$'s for $N = 76$, 78, and back-bending followed by up-bending at higher frequencies take place for $N = 80$.

In Fig. 11 are shown comparisons between $\mathcal{J}^{(1)}$ values inferred up to spin $I = 16\hbar$ from the data compilation [48–53] and from present predictions. As can be seen, the isotopes with $N = 70$–74 show experimental $\mathcal{J}^{(1)}$'s (red symbols) which begin to up-bend at frequency above $\omega \approx 0.3$ MeV. Back-bending is established for $N = 76$, 78 for ω higher than $\omega \approx 0.5$ MeV. The data above this frequency are not shown in panels (d) and (e) because the actual $\mathcal{J}^{(1)}$ values take on values stronger than 50 $\hbar^2$MeV^{-1}, the higher limit set in all the plots. Finally, back- and up-bendings take place in the $\mathcal{J}^{(1)}$ values for $N = 80$ at $\omega > 0.5$ MeV.

The $\mathcal{J}^{(1)}$ predictions at low spins and rotational frequencies display patterns similar to those for experimental values. The $\mathcal{J}^{(1)}$'s calculated for ^{130}Nd are smoothly increasing with increasing ω. For higher-mass isotopes, $72 < N < 80$, the moments of inertia start to display up-bending features which develop gradually with increasing mass. Back-bendings followed by up-bendings take place for ^{140}Nd. All these unexpected properties are not well understood, considering that the 5DCH theory is based on the adiabatic approximation, which implies that proton and neutron pairing energies retain unaltered their mean field HFB values while nuclei undergo rotational motion. From this discussion and comparison between experimental and calculated moments of inertia, it is safe to consider that the present 5DCH theory implemented with D1S is appropriate for the analyses of spectroscopic measurements for spins lower than $I = 10\hbar$ in the present study.

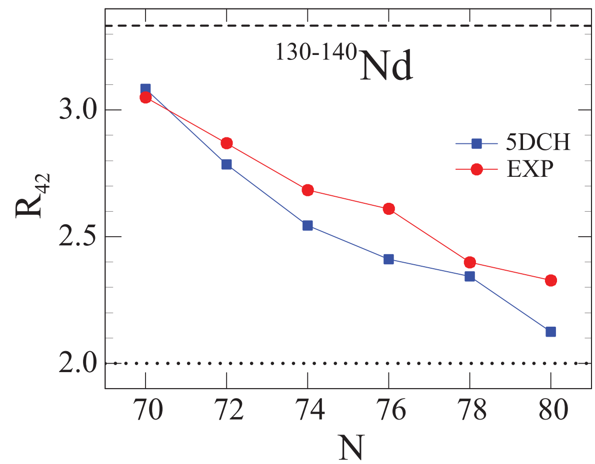

FIG. 12. Ratio of 4^+ and 2^+ excitation energies (MeV) of Nd gs-band levels as a function of neutron number. Red and blue symbols are for experimental and calculated values, respectively. The dashed and dotted lines are for rotational and vibrational R_{42} limits, respectively.

D. Ground state bands: Shape evolution and collectivity

1. Structure

The deformed-to-spherical shape transition from ^{130}Nd to ^{140}Nd is illustrated in Fig. 12 where we show the energy ratios $R_{42} = E(4_1^+)/E(2_1^+)$, with $E(4_1^+)$ and $E(2_1^+)$ being excitation energies of the 4^+ and 2^+ levels in the ground state bands, respectively. Both experimental values taken from [48–53] and 5DCH predictions display a regular decrease pattern with increasing N. None reaches the vibrational ($R_{42} = 2.0$) or rotational ($R_{42} = 3.3$) limit. The present comparison supports a previous statement according to which a first-order phase transition description is not applicable in the $N < 82$ region [6].

2. E2 transitions

Values of $B(E2)$ were measured previously for the $2_1^+ \longmapsto 0_1^+$, $4_1^+ \longmapsto 2_1^+$, $6_1^+ \longmapsto 4_1^+$, and $8_1^+ \longmapsto 6_1^+$ transitions in the neutron-deficient Nd region; see Refs. [48–53]. This data set together with that obtained in the present experimental work for ^{136}Nd are shown as red symbols in panels (a), (b), (c), and (d) of Fig. 13. A gradual reduction in strengths is observed

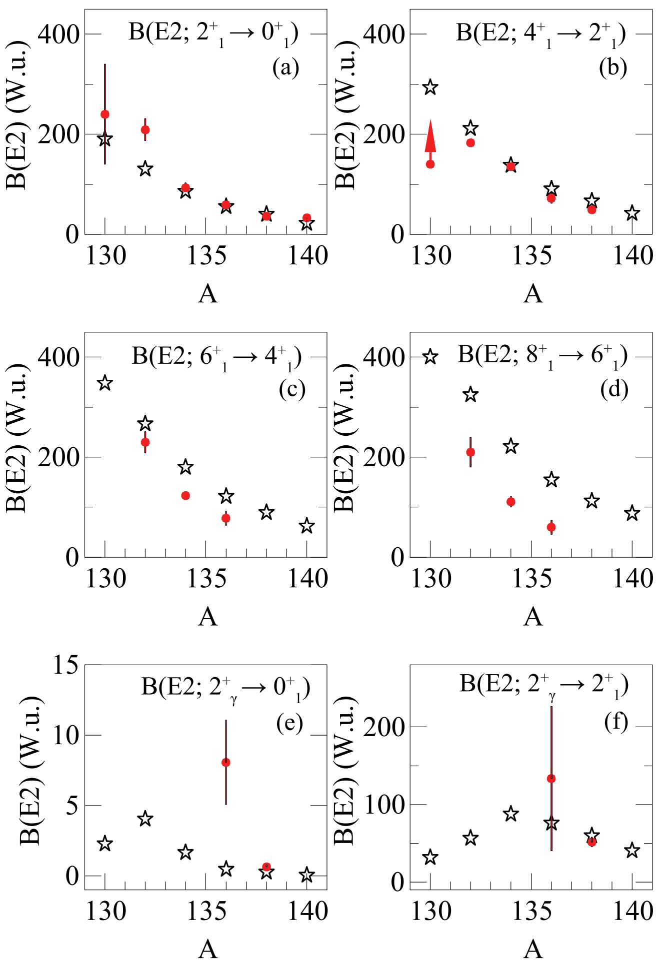

FIG. 13. $B(E2)$ strengths. Red and black symbols are for experimental and calculated values (W.u.), respectively. Panels (a)–(d) are for gs-band transitions. Panels (e) and (f) are for $\gamma \rightarrow$ gs transitions. For details see text.

as mass increases from $A = 130$ to $A = 140$. The $B(E2)$ predictions shown as black stars display similar patterns, in good agreement with data for the $2_1^+ \longmapsto 0_1^+$ and $4_1^+ \longmapsto 2_1^+$ transitions; see Table I. The agreement is worse for the $6_1^+ \longmapsto 4_1^+$ transition and is poor for the $8_1^+ \longmapsto 6_1^+$ transition. In these cases, the predicted values are too strong when compared to measurements for ^{136}Nd and higher-mass Nd isotopes. The 5DCH theory probably reaches a limit in its predictive power for the Nd transitional isotopes of present interest.

E. γ-Band properties

1. Level schemes

Some levels forming γ bands in $^{130-138}$Nd isotopes have been identified previously [8,48–53]. The data are shown as red circles in Fig. 14 where they are compared to 5DCH predictions (black circles) forming band structures defined according to which $B(E2\downarrow)$ value is stronger for any downward $I \longrightarrow J$ transition. The 2_γ^+ head levels are lower in energies for $N = 72$ and $N = 74$, features fulfilled by both data and

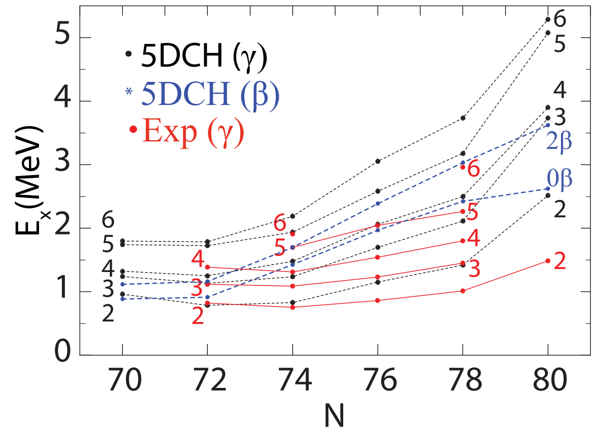

FIG. 14. Excitation energies (MeV) of γ-band levels up to spin $I = 8\hbar$. The red and black circles are for experimental and calculated values, respectively. The blue symbols are for 0_β^+ and 2_β^+ members of β-vibrational bands.

calculations. There is a fairly good agreement between both sets except for the heavier isotopes with $N > 76$.

2. Even-odd staggering

The γ-band staggering parameter $S(I)$, defined as [54]

$$S(I) = \frac{[E(I) - E(I-1)] - [E(I-1) - E(I-2)]}{E(2_1^+)},$$

usually serves as a measure of stiffness against γ deformation. The $S(I)$ patterns are shown for ^{130}Nd to ^{140}Nd in panels (a)–(f) of Fig. 15, where the sparse experimental data are shown as red squares. Analyses of the 5DCH predictions lead to identification of the γ-band members as the (2_2^+, 3_1^+, 4_2^+, 5_1^+, and 6_2^+) levels in $^{130-140}$Nd. The predicted $S(I)$ values (black squares) in panels (a)–(f) display zigzag features with $S(5) > S(4)$, in agreements with available data. In Fig. 15 are also shown $S(I)$ values inferred from asymmetric rotor model calculations [55]. All the $S(I)$ patterns are out of phase, with $S(5) < S(4)$, as compared with those from the 5DCH calculations. By analogy with the predictions in Fig. 8 showing band stretching with increasing angular momentum, we suggest that the $S(I)$ values from 5DCH calculations bring support to the interpretation that softness against triaxial deformation plays a key role in the low energy properties of $^{132-140}$Nd.

3. γ-to-gs Band E2 transitions

$B(E2; 2_\gamma^+ \longmapsto 0_1^+)$ and $B(E2; 2_\gamma^+ \longmapsto 2_1^+)$ strengths have been measured previously for ^{138}Nd [8] and for ^{136}Nd [10]. The latter data were obtained in rather "unsafe" Coulomb excitation measurements from which the $\gamma \longmapsto$ gs transition strengths were deduced relative to that measured for $B(E2; 2_1^+ \longmapsto 0_1^+)$, all characterized by large uncertainties. In the present study, the two interband transition strengths have been renormalized considering, instead, the precise $B(E2; 2_1^+ \longmapsto 0_1^+)$ value shown in Table I. As a result the formerly published $\gamma \longmapsto$ gs $E2$ transition strengths are now reduced by approximately 30%. These ^{136}Nd values as well as those measured previously for ^{138}Nd are displayed in

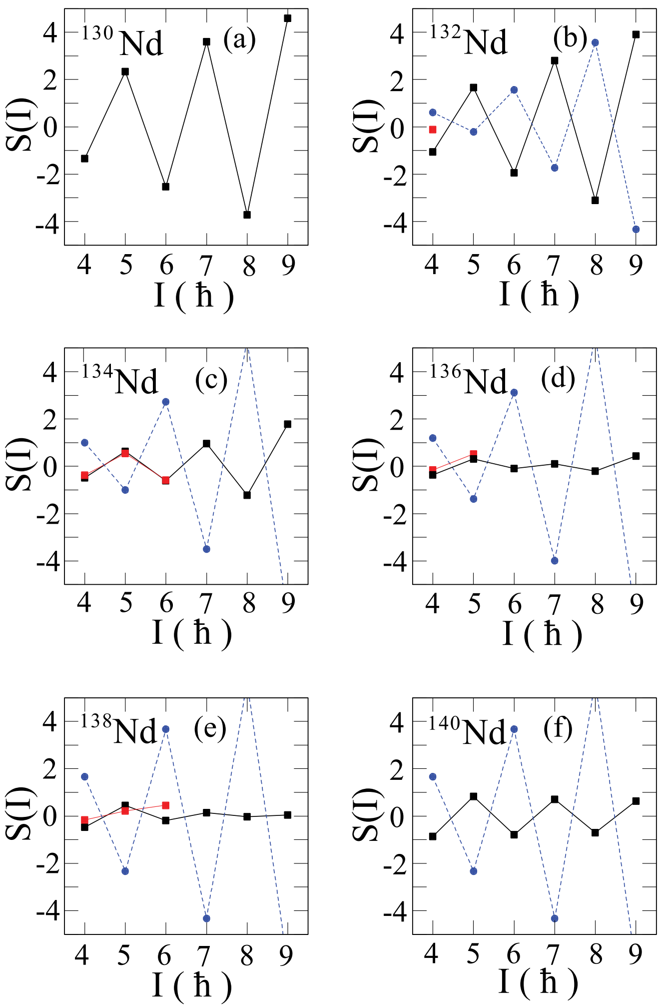

FIG. 15. Experimental and calculated even-odd staggering parameter $S(I)$ values are shown as red and black symbols, respectively. The blue symbols are for asymmetric rotor model predictions.

Figs. 13(e) and 13(f) as red symbols. Only for ^{138}Nd do the 5DCH predictions matching the data properly. New precise measurements, in particular for ^{134,136}Nd, will be assets to further challenge the present model predictions.

4. Branching ratios

Data for branching ratios $B(E2; 2^+_\gamma \longmapsto 0^+_1)/B(E2; 2^+_\gamma \longmapsto 2^+_1)$, as inferred from measurements compiled in the Evaluated Nuclear Structure Data File (ENSDF) [48–53], were used previously as testing grounds for interacting boson model (IBM) calculations relevant to the $^{132-140}$Nd isotopes [56]. The experimental values are marked as red symbols in Fig. 16, where they are compared to 5DCH predictions shown as blue symbols. Both sets display patterns weakening in magnitude with increasing neutron number. The predicted ratio evolution with increasing N is strongly correlated with that displayed by the $B(E2; 2^+_\gamma \longmapsto 0^+_1)$ values [see Fig. 13(e)].

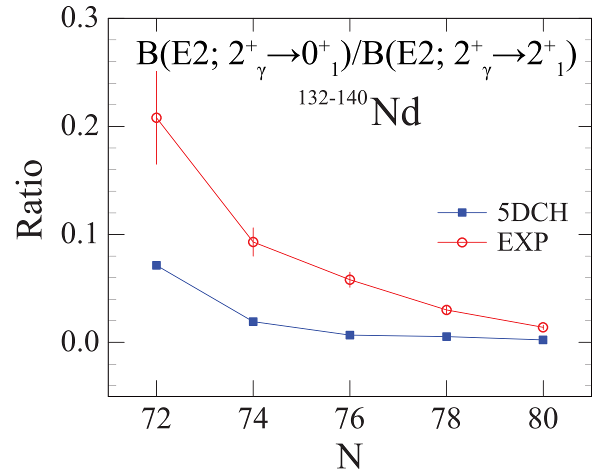

FIG. 16. $B(E2)$ ratio for γ- to gs-band transitions. Experimental and calculated values are shown as red and blue symbols, respectively.

5. Spectroscopic quadrupole moments

Spectroscopic quadrupole moments $Q(2^+_1)$ measured for the first 2^+ nuclear levels provide unambiguous information on their prolate or oblate character. One measurement is available in the Nd isotopes, namely ^{140}Nd for which $Q(2^+_1) = -0.48(31)$ eb [9]. This negative sign implies a prolate deformation, in agreement with the $Q(2^+_1)$ prediction shown as a black symbol in Fig. 17. All $Q(2^+_1)$ (black symbols) calculated for $N = 70$ to $N = 80$ display negative signs, the one stronger in magnitude being that for the most deformed, ^{130}Nd, among the Nd isotopes.

In Fig. 17 are also shown as blue symbols the Q predictions for the γ-bandhead levels, $Q(2^+_\gamma)$. For axially symmetric deformed nuclei considered in [57] and for rigid triaxial nuclei [55], $Q(2^+_1)$ and $Q(2^+_\gamma)$ are expected to display opposite signs. This property is fulfilled by present predictions through the isotopic Nd chain, including the well deformed lighter-mass $^{124-128}$Nd nuclei (not shown).

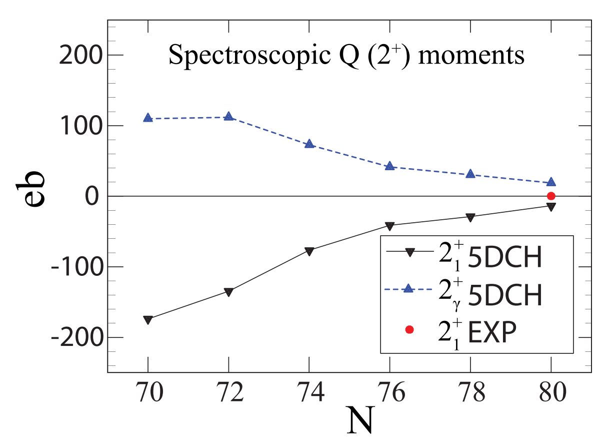

FIG. 17. Spectroscopic quadrupole moments (eb). Red symbol is for the ^{140}Nd experimental $Q(2^+_1)$ value. Black and blue symbols are for calculated $Q(2^+_1)$ and $Q(2^+_\gamma)$ values, respectively.

F. β-Vibrational levels

In contrast to the transitional character discussed above for the $^{130-140}$Nd isotopes, ^{150}Nd is a well deformed nucleus where gs- and β-vibrational bands were identified in experiments [48–53]. So are 5DCH predictions, with $\mathcal{J}^{(1)}$ values displaying smooth and regular patterns as angular momentum increases, at least up to $I = 8$. For the β-vibrational bands in neutron-deficient Nd isotopes, the calculated $\mathcal{J}^{(1)}$'s display no regular pattern at all, with increasing spins due to interaction with the γ band. As a matter of fact, the wave function components of the 2_3^+, 4_3^+, and 6_3^+ levels, which might be members of the hypothetical β-band built on top of the 0_2^+ level, exhibit a strong K mixing.

The 0_2^+ and 2_3^+ levels are shown as blue symbols in Fig. 14. Collectivity conveyed by $B(E2)$ strengths has been evaluated through $B(E2; 2_\beta^+ \longmapsto 0_\beta^+)$ calculations for the purpose of comparison with those for $2_1^+ \longmapsto 0_1^+$ transitions. The ratio

$$R_B = \frac{B\big(E2; 2_\beta^+ \longmapsto 0_\beta^+\big)}{B(E2; 2_1^+ \longmapsto 0_1^+)}$$

takes on values 0.71, 1.27, 1.79, 1.68, 1.58, and 1.66 for mass increasing from $A = 130$ to $A = 140$. The ratio is maximal for ^{134}Nd. It is hoped that present predictions will be challenged in future experiments.

G. Shape coexistence

Shape coexistence in nuclei is usually suggested by secondary potential minima present in potential energy surfaces. Despite the fact that none can be identified in Fig. 7, some features indicating shape coexistence phenomena may still be sought in the Nd isotopes by considering $E0$ transitions. $\rho^2(E0)$ rates for $0_2^+ \longmapsto 0_1^+$ transitions provide measures of how strong $E0$ transitions might be, as discussed previously in the geometric model [58] as well as in dedicated algebraic models [59,60]. Both models suggest relationships taking place between $E0$ transitions and isotope and isomer shifts. Here $\rho^2(E0)$ rates, isotope shifts, and isomer shifts are obtained in 5DCH calculations. Next, the comparison between $\rho^2(E0)$ rates with those inferred from isomer shifts is discussed.

1. Charge radii and isotope shifts

The 5DCH values for charge radii and isotope shifts are displayed in Figs. 18(a) and 18(b), where measurements [61,62], shown as red symbols, are compared to calculations conducted for $N = 70$ to $N = 90$. Good agreement is obtained for the radii, except in the vicinity of the $N = 82$ shell closure. This was expected since the nucleon numbers N and Z are constrained to their mean $\langle N\rangle$ and $\langle Z\rangle$ values in the HFB calculations, the first stages involved in the 5DCH theory. This caveat in charge radius prediction propagates into the isotope shift calculations which display a systematic lowering as compared to data shown in Fig. 18(b).

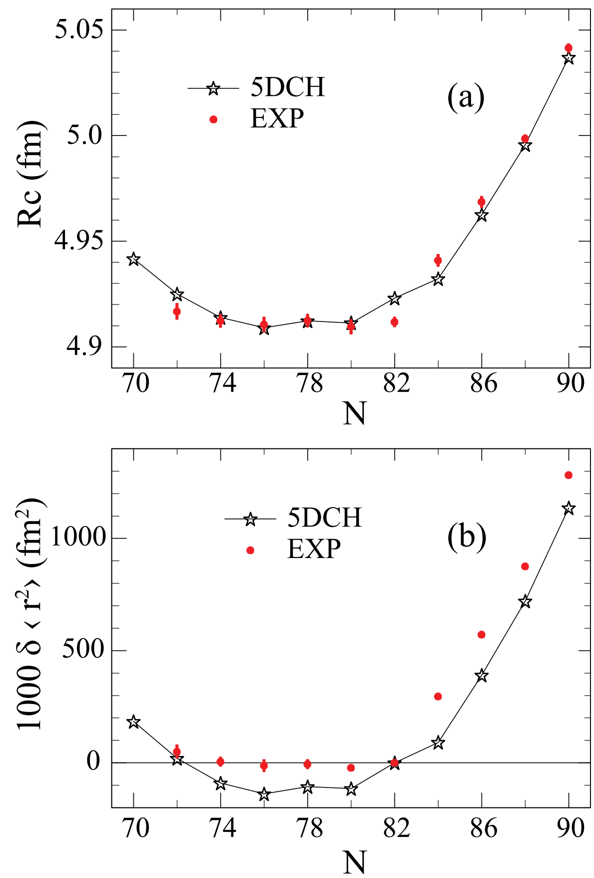

FIG. 18. Panels (a) and (b) are for charge radii and isotope shifts, respectively. Red and black symbols are for experimental and calculated values, respectively.

2. E0 transitions

$0_2^+ \longmapsto 0_1^+$ transition rates are calculated as specified in [44]. The 5DCH results (blue symbols) are displayed in Fig. 19 as functions of N from $N = 70$ to $N = 90$. The $\rho^2(E0)$ rates take on strong values at lower and higher N, and reach, for ^{142}Nd, a minimum close to the experimental value $1000\rho^2(E0) = 17 \pm 6$ as quoted in Ref. [58].

The relationship between $E0$ transition rates and isomer shifts is discussed in [58]. We make use of the same definition, namely

$$\rho^2(E0) = \frac{Z^2}{R_0^4}\alpha^2(1-\alpha^2)|\Delta\langle r^2\rangle|^2,$$

as that published therein for calculating the inferred $\rho^2(E0)$ rates. The isomer shifts $\Delta\langle r^2\rangle$ are determined from 5DCH calculations and combined with the mixing amplitude α taken at the maximum value $1/\sqrt{2}$ to calculate $E0$ rates. Results are shown as open squares in Fig. 19. Good agreement between $E0$ data and the two model calculations is obtained for $N = 82$. Furthermore, $E0$ rates calculated following the two methods match each other reasonably well for $78 < N < 86$, indicating that the approximation of Wood *et al.* is appropriate for weakly deformed nuclei.

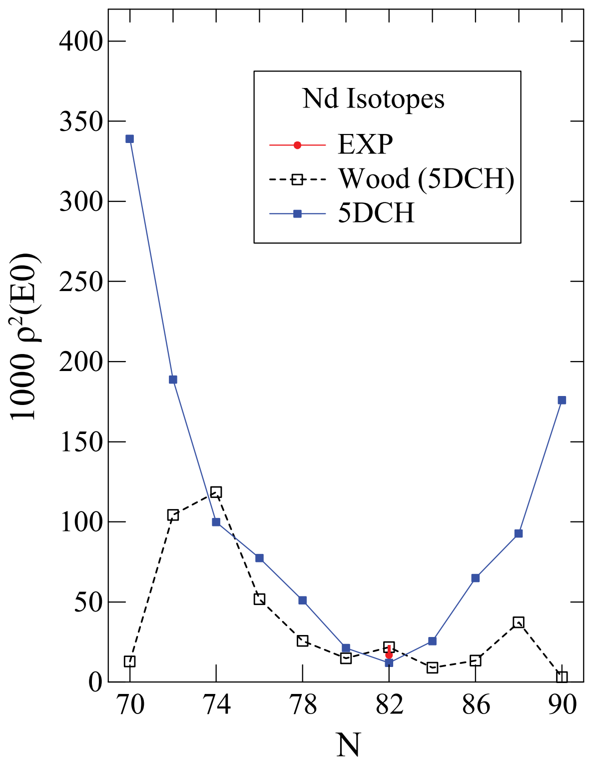

FIG. 19. $E0$ transitions. Calculated $\rho^2(E0)$ rates (blue symbols) versus neutron numbers, from $N = 70$ to $N = 90$. The red symbol is the experimental value measured for ^{142}Nd. Open squares are for $\rho^2(E0)$ values determined from calculated isomer shifts.

VI. SUMMARY AND CONCLUSION

Precision lifetime measurements of the yrast states in ^{136}Nd have been performed up to spin $I = 14\hbar$ using the recoil distance Doppler shift technique following the ^{124}Te(^{16}O, $4n$) nuclear reaction. The lifetime of the first 2^+ state has also been measured using the in-beam fast timing method in order to support the RDDS measurement. In addition, lifetimes for several negative parity band levels were measured. The deduced intraband $B(E2)$ values are valuable assets for understanding the nuclear structure at low excitation energy and spins available for the $^{130-140}$Nd isotopes.

A comprehensive and systematic study of all even-even neutron-deficient Nd isotopes based on the microscopic 5DCH theory implemented with the D1S force is performed. Predictions are challenged through comparisons with data for gs and γ bands, kinetic moments of inertia, $B(E2)$ strengths for intra- and interband transitions, quadrupole spectroscopic factors, charge radii and isotope shifts, and $E0$ transitions. An overall agreement between measurements and calculations is obtained, shedding new light on the collective structure properties of the neutron-deficient transitional γ-soft Nd isotopes. More measurements are called for, especially those dedicated to $\gamma \longmapsto$ gs transitions, spectroscopic quadrupole moments, and $E0$ transition rates that serve as indicators of shape coexistence phenomena.

The 5DCH predictions need improvements for the gs intraband transitions, which significantly overestimate in a systematic way the $B(E2; 8_1^+ \longmapsto 6_1^+)$ and $B(E2; 6_1^+ \longmapsto 4_1^+)$ measured values. Too strong collectivity in predictions may indicate the need for adding two or more quasiparticle components in the model wave functions [15]. A few studies devoted to coupling of two-quasiparticles (2qp) to collective excitations in several mass regions including the neutron-deficient Nd isotopes, have already been performed [63–68]. It would be interesting to extend the generator coordinate method implemented with Gogny force by including 2qp components in the energy density functional, as exposed in [69]. It is hoped that such a model extension will lead to reducing collectivity of yrast states in neutron-deficient Nd isotopes as angular momentum increases.

ACKNOWLEDGMENTS

This work was supported by the Ministry of Education and Research of Romania, CNCS-UEFISCDI through Contract No. PN19060102. We would like to thank the technical staff from the 9MV Tandem accelerator in IFIN-HH for their support during the experiment.

[1] P. Möller, R. Bengtsson, B. G. Carlsson, P. Olivius, and T. Ichikawa, Phys. Rev. Lett. **97**, 162502 (2006).
[2] I. Ragnarsson, A. Sobiczewski, R. K. Sheline, S. E. Larsson, and B. Nerlo-Pomorska, Nucl. Phys. A **233**, 329 (1974).
[3] B. D. Kern, R. L. Mlekodaj, G. A. Leander, M. O. Kortelahti, E. F. Zganjar, R. A. Braga, R. W. Fink, C. P. Perez, W. Nazarewicz, and P. B. Semmes, Phys. Rev. C **36**, 1514 (1987).
[4] N. Redon, J. Meyer, M. Meyer, P. Quentin, M. S. Weiss, P. Bonche, H. Flocard, and P.-H. Heenen, Phys. Lett. B **181**, 223 (1986).
[5] M. O. Kortelahti, B. D. Kern, R. A. Braga, R. W. Fink, I. C. Girit, and R. L. Mlekodaj, Phys. Rev. C **42**, 1267 (1990).
[6] E. A. McCutchan, R. F. Casten, V. Werner, R. J. Casperson, A. Heinz, J. Qian, B. Shoraka, J. R. Terry, E. Williams, and R. Winkler, Phys. Rev. C **87**, 057306 (2013).
[7] J. Xiang, Z. P. Li, W. H. Long, T. Nikšić, and D. Vretenar, Phys. Rev. C **98**, 054308 (2018).
[8] F. L. Bello Garrote *et al.*, Phys. Rev. C **97**, 064310 (2018).
[9] C. Bauer *et al.*, Phys. Rev. C **88**, 021302(R) (2013).
[10] T. R. Saito *et al.*, Phys. Lett. B **669**, 19 (2008).
[11] A. Tucholski *et al.*, Phys. Rev. C **100**, 014330 (2019).
[12] S. Mukhopadhyay *et al.*, Phys. Rev. C **78**, 034311 (2008).
[13] C. M. Petrache *et al.*, Phys. Rev. C **97**, 041304(R) (2018).
[14] Y. Shi, Phys. Rev. C **99**, 034304 (2019).
[15] Y. K. Wang, F. Q. Chen, P. W. Zhao, S. Q. Zhang, and J. Meng, Phys. Rev. C **99**, 054303 (2019).
[16] N. M. Florea *et al.*, J. Radioanal. Nucl. Chem. **305**, 707 (2015).
[17] F. Pühlhofer, Nucl. Phys. A **280**, 267 (1977).
[18] J. Srebrny *et al.*, Nucl. Phys. A **683**, 21 (2001).

[19] D. Bucurescu *et al.*, Nucl. Instrum. Methods Phys. Res. A **837**, 1 (2016)
[20] T. K. Alexander and J. S. Forster, Adv. Nucl. Phys. **10**, 197 (1978).
[21] A. Dewald, O. Möller, and P. Petkov, Prog. Part. Nucl. Phys. **67**, 786 (2012).
[22] J. Billowes, K. P. Lieb, J. W. Noe, W. F. Piel, S. L. Rolston, G. D. Sprouse, O. C. Kistner, and F. Christancho, Phys. Rev. C **36**, 974 (1987).
[23] P. Petkov, D. Tonev, J. Gableske, A. Dewald, T. Klemme, and P. von Brentano, Nucl. Instrum. Methods Phys. Res. A **431**, 208 (1999).
[24] G. Winter, ZfK Rossendorf Report ZfK-497, 1983 (unpublished); Nucl. Instrum. Methods **214**, 537 (1983).
[25] P. Petkov *et al.*, Nucl. Phys. A **640**, 293 (1998).
[26] L. C. Northcliffe and R. F. Schilling, Nucl. Data Tables **7**, 233 (1970).
[27] J. F. Ziegler and W. K. Chu, At. Data Nucl. Data Tables **13**, 463 (1974).
[28] J. F. Ziegler and J. P. Biersack, in *Treatise on Heavy-Ion Science*, edited by D. A. Bromley (Plenum, Oxford, 1985), Vol. 6, p. 95
[29] J. Lindhard, M. Scharff, and H. E. Schiøtt, K. Dan. Vidensk. Selsk. Mat. Fys. Medd. **33**, 1 (1963).
[30] W. M. Currie, Nucl. Instrum. Methods **73**, 173 (1969).
[31] J. Keinonen, Capture Gamma-ray spectroscopy and related topics–1984, in *Proceedings of the Fifth International Symposium, Knoxville, Tennessee*, edited S. Raman, AIP Conf. Proc. No. 125 (AIP, New York, 1985), p. 557.
[32] P. Petkov *et al.*, Nucl. Phys. A **674**, 357 (2000).
[33] A. Dewald, S. Harissopulos, and P. von Brentano, Z. Phys. A **334**, 163 (1989).
[34] G. Böhm, A. Dewald, P. Petkov, and P. von Brentano, Nucl. Instrum. Methods Phys. Res. A **329**, 248 (1993).
[35] P. Petkov, Nucl. Instrum. Methods Phys. Res. A **349**, 289 (1994).
[36] E. S. Paul, C. W. Beausang, D. B. Fossan, R. Ma, W. F. Piel, Jr., P. K. Weng, and N. Xu, Phys. Rev. C **36**, 153 (1987)
[37] H. J. Wollersheim *et al.*, Nucl. Instrum. Methods Phys. Res. A **537**, 637 (2005).
[38] J. Mierzejewski *et al.*, Nucl. Instrum. Methods Phys. Res. A **659**, 84 (2011).
[39] N. Marginean *et al.*, Eur. Phys. J. A **46**, 329 (2010).
[40] R. Lica, U.P.B. Sci. Bull. **78**, 263 (2016).
[41] C. Wheldon, http://www.np.ph.bham.ac.uk/research_resources/programs/.
[42] S. Pascu *et al.*, Phys. Rev. C **91**, 034321 (2015).
[43] P. Petkov *et al.*, Nucl. Phys. A **957**, 240 (2017).
[44] J.-P. Delaroche, M. Girod, J. Libert, H. Goutte, S. Hilaire, S. Péru, N. Pillet, and G. F. Bertsch, Phys. Rev. C **81**, 014303 (2010).
[45] J. Dechargé and D. Gogny, Phys. Rev. C **21**, 1568 (1980).
[46] J.-F. Berger, M. Girod, and D. Gogny, Comput. Phys. Commun. **63**, 365 (1991).
[47] J. Libert, M. Girod, and J.-P. Delaroche, Phys. Rev. C **60**, 054301 (1999).
[48] B. Singh, Nucl. Data Sheets **93**, 33 (2001).
[49] Yu. Khazov, A. A. Rodionov, S. Sakharov, and B. Singh, Nucl. Data Sheets **104**, 497 (2005).
[50] A. A. Sonzogni, Nucl. Data Sheets **103**, 1 (2004).
[51] E. A. Mccutchan, Nucl. Data Sheets **152**, 331 (2018).
[52] J. Chen, Nucl. Data Sheets **146**, 1 (2017).
[53] N. Nica, Nucl. Data Sheets **154**, 1 (2018).
[54] N. V. Zamfir and R. F. Casten, Phys. Lett. B **260**, 265 (1991).
[55] A. S. Davidov and G. F. Filipov, Nucl. Phys. **8**, 237 (1958).
[56] S. Pascu, N. V. Zamfir, G. Căta-Danil, and N. Mărginean, Phys. Rev. C **81**, 054321 (2010).
[57] A. Bohr and B. R. Mottelson, *Nuclear Structure* (W. A. Benjamin, Reading, MA, 1975), Vol. II.
[58] J. L. Wood, E. F. Zganjar, C. De Coster, and K. Heyde, Nucl. Phys. A **651**, 323 (1999), and references therein.
[59] K. Heyde and J. L. Wood, Rev. Mod. Phys. **83**, 1467 (2011).
[60] S. Zerguine, P. Van Isacker, and A. Bouldjedri, Phys. Rev. C **85**, 034331 (2012).
[61] I. Angeli, At. Data Nucl. Data Tables **87**, 185 (2004).
[62] I. Angeli and K. P. Marinova, At. Data Nucl. Data Tables **99**, 69 (2013).
[63] M. Didong, H. Müther, K. Goeke, and A. Faessler, Phys. Rev. C **14**, 1189 (1976).
[64] H. Müther, K. Goeke, K. Allaart, and A. Faessler, Phys. Rev. C **15**, 1467 (1977).
[65] A. A. Raduta, C. Lima, and A. Faessler, Phys. Lett. B **121**, 1 (1983).
[66] G. L. Long, Phys. Rev. C **55**, 3163 (1997).
[67] D. S. Chuu, S. T. Hsieh, and H. C. Chiang, Phys. Rev. C **40**, 382 (1989).
[68] D. Vretenar, S. Brant, G. Bonsignori, L. Corradini, and C. M. Petrache, Phys. Rev. C **57**, 675 (1998).
[69] F.-Q. Chen and J. L. Egido, Phys. Rev. C **95**, 024307 (2017).